MATEC Web of Conferences **123**, 00027 (2017) DOI:10.1051/matecconf/201712300027
ICPMMT 2017

Preparation and properties of the (Sr,Ba)Nb_2O_6 thin films by using the sputtering method

Chien-Chen Diao[1], *Cheng-Fu* Yang[2], and *Chia-Ching* Wu[1,*]

[1] Department of Electronic Engineering, Kao Yuan University, Kaohsiung, Taiwan
[2] Department of Chemical and Materials Engineering, National University of Kaohsiung, Kaohsiung, Taiwan

Abstract. Strontium barium niobate ($Sr_{0.3}Ba_{0.7}Nb_2O_6$, SBN) thin films were deposited on silicon substrate by using the radio frequency magnetron sputtering and under different deposition power and time at room temperature. Surface morphology and thicknesses of the SBN thin films were characterized by field emission scanning electron microscopy. The crystallization films at different deposition power and time were analyzed by X-ray diffraction (XRD) using CuKα radiation from a Rigaku rotating anode with an incident angle of 2°. The remnant polarization (Pr), saturation polarization (Ps), and minimum coercive field (Ec) properties of the metal-ferroelectric-metal (MFM) structure were measured using ferroelectric material test instrument. The SBN thin films deposited at 90 min and 125 W had the maximum Pr, Ps, and minimum Ec of 1.26 $\mu C/cm^2$, 2.41 $\mu C/cm^2$, and 201.6 kV/cm, respectively. From above results, it knows that the SBN thin films suit for application on ferroelectric random access memory (FeRAM).

1 Introduction

Ferroelectric materials are an important class of materials whose main characteristic is the presence of a spontaneous polarization that can be changed with an external electric field. The tungsten bronze family is one of several ferroelectric materials that includes niobates such as (Sr,Ba)Nb_2O_6 (SBN), (Pb,Ba)Nb_2O_6 (PBN) and (Pb,K)Nb_2O_6 (PKN). In February 2003, the European Union adopted the Restriction of Hazardous Substances (RoHS) directive, limiting the use of certain hazardous substances in electrical and electronic equipment. In accordance with environmental concerns and to avoid problems related to use of lead (Pb), researchers have moved toward using lead-free materials. The SBN is a lead-free ferroelectric material, widely considered very useful in diverse device applications, including memory devices [1], waveguide devices [2], and others. An important representing of ferroelectric material is the SBN, known by excellent pyroelectric coefficient [3, 4], piezoelectric [5] and electro optic properties [6, 7]. SBN presents a tetragonal or orthorhombic phase, depending of composition and temperature.

The SBN solid-solution series crystallize in the tetragonal tungsten bronze (TTB) structure. At room temperature it has the symmetry of the space group P4bm for $0.25 < x < 0.75$. It belongs to the 4mm point group in the ferroelectric phase and changes to the 4/mmm when in the paraelectric phase. Investigation of $Sr_xBa_{1-x}Nb_2O_6$ ceramics using X-ray diffraction suggests that a morphotropic phase boundary (MPB) exist at round the composites of $Sr_{0.25}Ba_{0.75}Nb_2O_6$, which is characterized by the coexistence of the tetragonal and orthorhombic phases [8]. $Sr_{0.2}Ba_{0.8}Nb_2O_6$ ceramic presents a tetragonal ferroelectric phase between 120 and 293°C, an orthorhombic phase below 120°C and a tetragonal paraelectric phase above 293°C.

SBN thin films have been prepared by several techniques like sol-gel processing [9], pulsed laser deposition [10] and metalorganic chemical vapor deposition (MOCVD) [11]. Recently, it has been proposed to prepare SBN thin films by a chemical method based on a polymeric resin containing metallic ions [12]. However, the radio frequency (RF) magnetron sputtering is a simple method to deposit the needed thin films [13]. In the research, $Sr_{0.7}Ba_{0.3}Nb_2O_6$ (SBN) thin films were obtained by a radio frequency (RF) magnetron sputtering method at room temperature. The influence of deposition power and time on the crystallinity and ferroelectricity of SBN thin films was studied using the analysis of scanning electron microscopy and X-ray diffraction, and the measured of leakage current and polarization, respectively.

2 Experimental procedures

The conventional solid-state reaction method was used to prepare the $Sr_xBa_{1-x}Nb_2O_6$, x=0.3 (SBN) ceramic. Reagent-grade oxide or carbonate powders of $SrCO_3$, $BaCO_3$, and Nb_2O_5 with greater than 99.5% purity were used as starting raw materials. The oxides were mixed with deionized water by ball-milling for 1 h. After drying and grinding, the powder was calcined at 1100 °C for 2 h, and the formation of the tungsten bronze structure was confirmed by the XRD pattern. Then, ground again and mixed with polyvinyl alcohol (PVA)

---

[*] Corresponding author: t10068@cc.kyu.edu.tw

as binder. the calcined powder was uniaxially pressed in a steel die into a 2-inch disk, and the ceramic was sintered at 1340 °C in air for 2 h. The SBN thin films were deposited under various deposition power and time on a silicon wafer by an radio frequency (RF) sputtering method. The deposition pressure was 5×10^{-3} torr, and pure argon (Ar) was used as the reaction gas. Finally, the aluminum (Al) top electrodes were deposited by an electron beam evaporation method on the SBN thin films, with a 1 mm diameter shadow mask, to form the metal-ferroelectric-metal (MFM) structures. The structure of the SBN ceramic and thin films were analyzed by X-ray diffraction (XRD) using CuKα radiation from a Rigaku rotating anode with an incident angle of 2°. Field emission scanning electron microscopy (FE-SEM) was used to study the surface morphologies of the SBN ceramic and thin films. The leakage current density versus applied electric field (J-E) was measured using an HP 4156 semiconductor parameter analyzer. The saturation polarization, remanent polarization, and coercive field properties of the MFM structure were measured using ferroelectric material test instrument.

3 Results and discussion

The FE-SEM morphology of 1340 ºC sintered SBN ceramic as shown in Fig. 1. In Fig. 1, as the SBN ceramic sintered at 1340°C, the several bar-type grains developed and no any pores are observed. Figure 2 shows the X-ray diffraction (XRD) patterns of 1340 ºC sintered SBN ceramic in the 2θ range of 20 to 80^{o} as shown in Fig. 2. The XRD results revealed at 2θ values of 22.4^{o}, 25.6^{o}, 27.6^{o}, 28.3^{o}, 29.3^{o}, 30.3^{o}, 31.9^{o}, 34.2^{o}, 36.6^{o}, 38.9^{o}, 42.1^{o}, 45.8^{o}, 48.7^{o}, 49.4^{o}, 51.5^{o}, 52.3^{o}, 53.5^{o}, 54.3^{o}, 55.4^{o} and 57.1^{o} were corresponded to the (001), (320), (221), (440), (410), (221), (331), (321), (401), (520), (530), (260), (630), (601), (550), (541), (332), (631), (412) and (711) planes of SBN ceramic, respectively. No second phase was present in this ceramic.

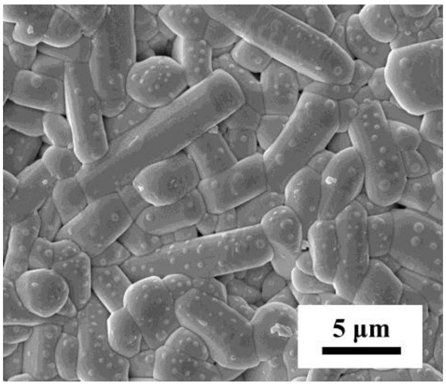

Fig. 1. SEM images of the SBN ceramic sintered at 1340 ºC.

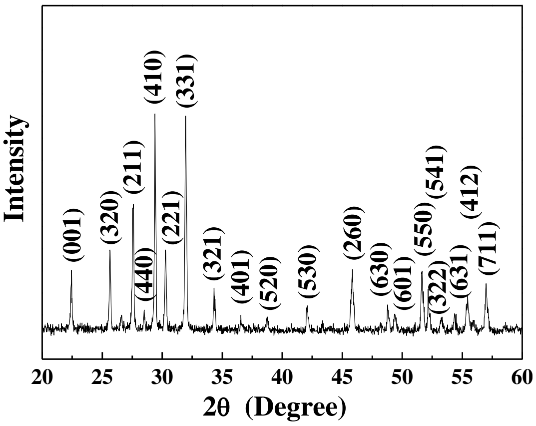

Fig. 2. XRD patterns of the SBN ceramic sintered at 1340 ºC.

Figure 3 shows the temperature dependence on the dielectric constants (ε_r-T) of the SBN ceramic sintered at 1340 ºC. It fount that the dielectric constant increased as the measured temperature increased at 135 ^{o}C, than, the dielectric constant decreased as the measured temperature increases from 140 to 200 ^{o}C. The SBN ceramic have a dielectric peak (K_{max}) at 135 ^{o}C, which is the Curie temperature (T_c) of SBN ceramic, and the maximum dielectric constant is ε_r=4322.

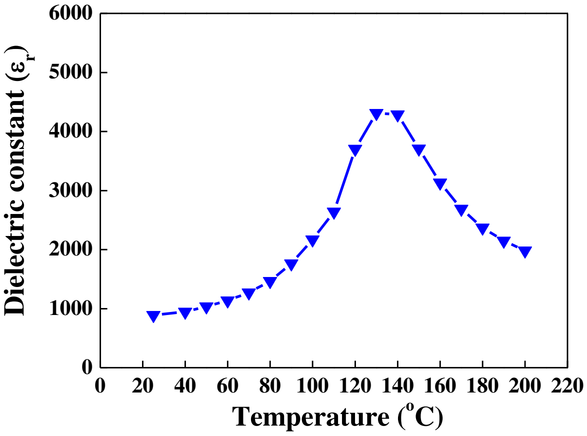

Fig. 3. Temperature dependence on the dielectric constants of the SBN ceramic sintered at 1340 ^{o}C.

Figure 4 shows surface FE-SEM images of the SBN thin films with different deposition power. The SBN surface morphology varies greatly with the different sputtering power, as shown in Fig. 4(a) to Fig. 4(d). In the case of the SBN thin film deposited at 75 W (Fig. 2(a)), the surface is smooth and no grain growth is observable. Because the kinetic energy of the sputtered particles arriving at the substrate surface is weak. As the deposition power increases from 75 W to 125 W, the surface roughness of the SBN thin films slightly increased, and no grain growth is observable. However, the grain in the SBN thin film was observed as the deposited power at 150 W.

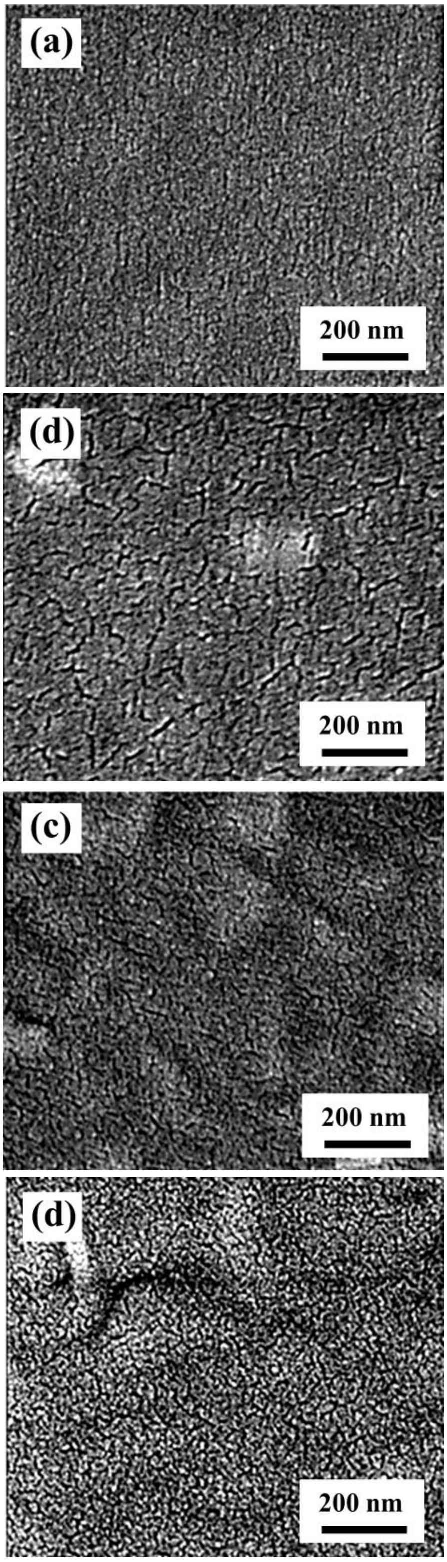

Fig. 4. SEM images of the SBN thin films deposited with different power. (a)75 W, (b)100 W, (c)125 W and (d)150 W.

Figure 5 shows the influence of deposition power on the thickness of the SBN thin films. At deposition power were 75, 100, 125 and 150 W, the thickness of the SBN thin films were 277.19, 333.33, 350.87, and 282.46 nm, respectively. The thinckness of the SBN thin films increased as the depoaition power increases from 75 W to 125 W. This results cause by the number of sputtered particles arriving at the substrate increased. As the deposition power increasing from 125 W to 150 W, the thinckness of the SBN thin film decreased. This results cause by the higher energy of sputtered particles arriving at the substrate and etching the film surface as the deposition power at 150 W.

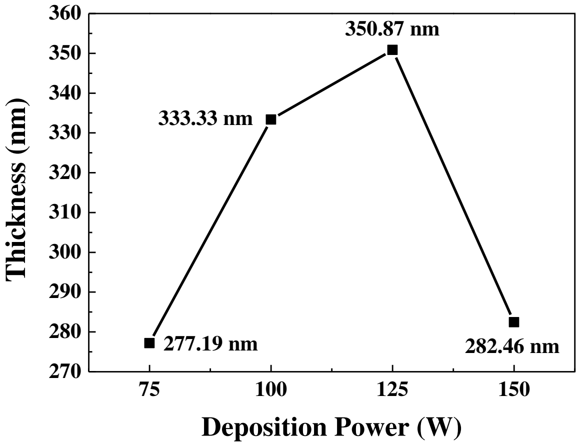

Fig. 5. Thickness of the SBN thin films deposited with different power.

The XRD analysis of the SBN thin films deposited at different power are shown in Fig. 6. All the SBN thin films showed an amorphous structure because they were deposited at room temperature. Figure 6(a) is the standard peak of the aluminum (Al). A crystalline peak of 38.5° is revealed in the Al electrode, and the diffraction peaks' intensity decreases as the deposition power increases from 75 to 150 W, as shown in Figs. 6(b) to 6(e). This result confirms that the thickness of the SBN thin films increases as the deposition power increases from 75 W to 150 W.

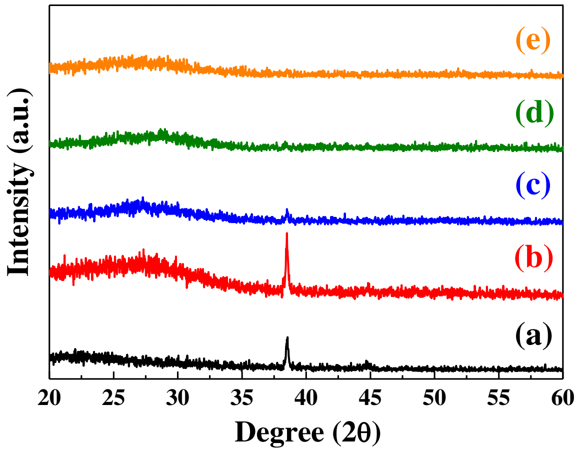

Fig. 6. XRD analysis of the SBN thin films deposited with different power. (a) standard peak, (b)75 W, (c)100 W, (d)125 W and (e)150 W.

Figure 7 shows the leakage current density versus electrical field (J-E) curves of the SBN thin films deposited with different power. The leakage current density of the SBN thin films slightly decreased as the deposition power increased from 75 W to 125 W. There are many reasons will influence the leakage current densify, including the thickness and defects of the deposited this films [14, 15].

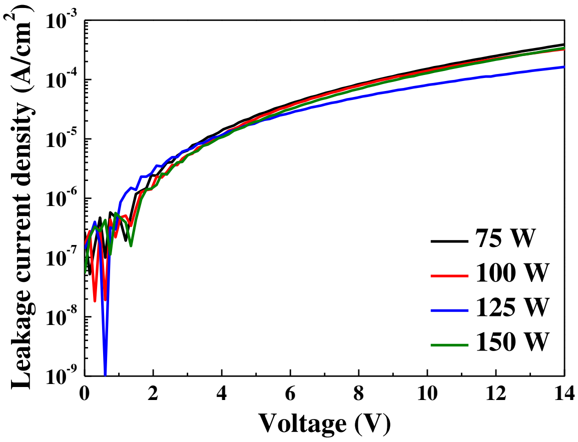

Fig. 7. Leakage current density of the SBN thin films deposited with different power.

Figure 8 shows surface FE-SEM images of the SBN thin films with different deposition time. In the case of the SBN thin film deposited at 30 min, the surface is smooth and no grain growth is observable as shown in Fig. 8. As the deposition time increases from 60 to 120 min, the surface roughness of the SBN thin films increased, and grain growth is observable at the 120 min deposition time.

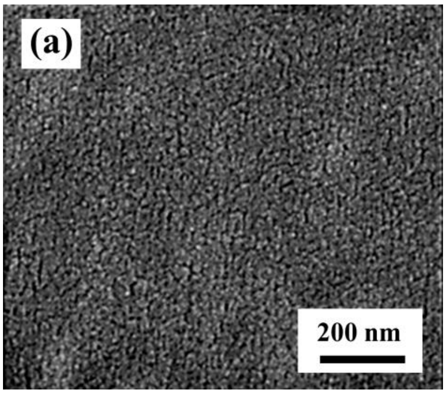

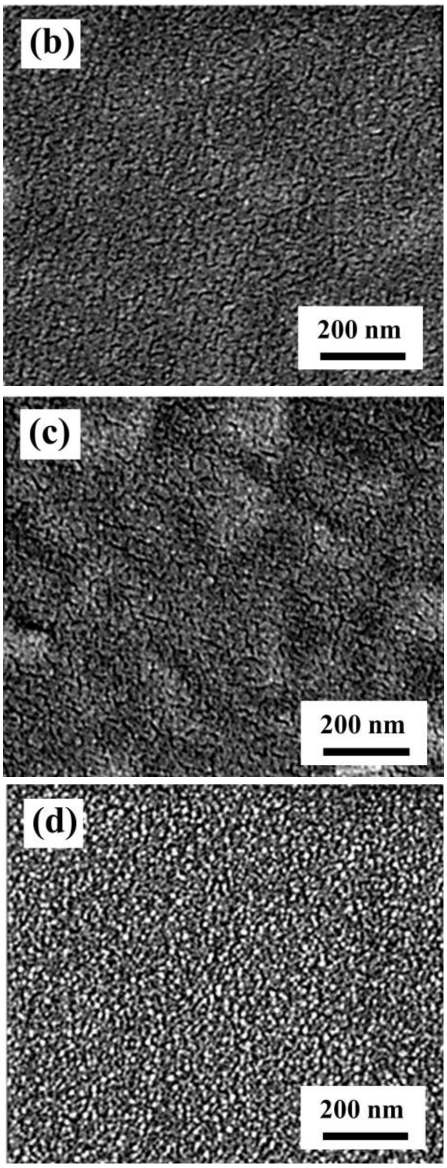

Fig. 8. SEM images of the SBN thin films deposited with different time. (a)30 min, (b) 60 min, (c) 90 min and (d) 120 min.

Figure 9 shows the influence of deposition time on the thickness of the SBN thin films. At deposition times were 30, 60, 90 and 120 min, the thickness of the SBN thin films were 175.43, 189.47, 292.98, and 350.87 nm, respectively. The thinckness of the SBN thin films increased as the depoaition times increases from 30 min to 120 min. This results cause by the number of sputtered particles arriving at the substrate increased as the deposition time increased.

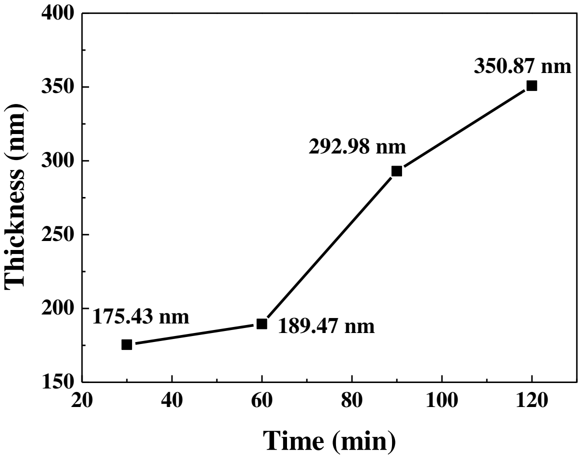

Fig. 9. Thickness of the SBN thin films deposited with different time.

The XRD analysis of the SBN thin films deposited at different time are shown in Fig. 10. All the SBN thin films showed an amorphous structure because they were deposited at room temperature. A crystalline peak of 38.5° is revealed in the Al electrode, and the diffraction peaks' intensity decreases as the deposition time increases from 30 min to120 min, as shown in Figs. 10(a) to 10(d). This result confirms that the thickness of the SBN thin films increases as the deposition time increases from 30 min to 120 min.

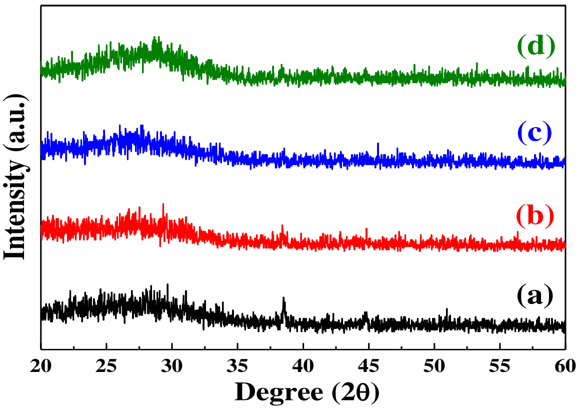

Fig. 10. XRD analysis of the SBN thin films deposited with different time. (a)30 min, (b) 60 min, (c) 90 min and (d) 120 min.

Figure 11 shows the leakage current density versus electrical field (J-E) curves of the SBN thin films deposited with different time. The leakage current density of the SBN thin films decreased as the deposition time increased from 30 min to 90 min. As the deposition at 120 min, the leakage current density of the SBN thin films slightly increased. The larger leakage current density led to less residual charge in the ferroelectric layer.

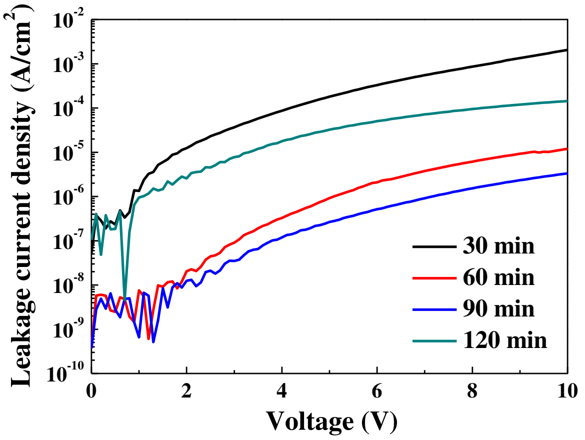

Fig. 11. Leakage current density of the SBN thin films deposited with different time.

Figure 12 shows the polarization versus applied electrical field (P-E) curves of the SBN thin film. The development of hysteresis loops in the SBN thin film confirms the ferroelectric nature. The SBN thin films deposited at 90 min and 125 W had the maximum remnant polarization (Pr), saturation polarization (Ps), and minimum coercive field (Ec) of 1.26 μC/cm^2, 2.41 μC/cm^2, and 201.6 kV/cm, respectively. The Pr, Ps and Ec values of the SBN thin film deposited at 90 min, 125 W and room temperature are slightly larger than those in other reports [22-24].

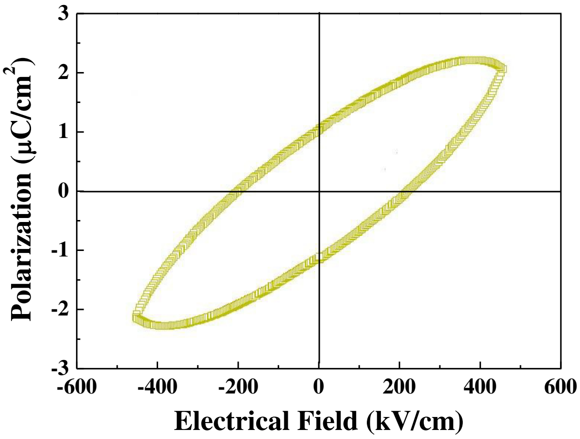

Fig. 12. Polarization versus electrical field curves of the SBN thin film deposited at 90 min and 125 W.

4 Conclusion

In this study, high-quality $Sr_{0.7}Ba_{0.3}Nb_2O_6$ (SBN) thin films were deposited on silicon wafer using an radio frequency (RF) magnetron sputtering. When 90 min and 125 W were used as deposition time and power, the smaller leakage current density of the SBN thin film was obtained. In addition, the remnant polarization (Pr), saturation polarization (Ps), and minimum coercive field (Ec) of 1.26 μC/cm^2, 2.41 μC/cm^2, and 201.6 kV/cm, respectively. We demonstrated that the SBN thin film will play an important role in applications for nonvolatile memory devices.

Acknowledgements

The authors acknowledge the financial support of the Ministry of Science and Technology, R.O.C. with the contract Nos. 105-2221-E-244-013- and 105-2221-E-244-014-.

References

1. M. C. Kuan, K. H. Chen, W. C. Tzou, C. M. Cheng, Y. J. Lin, *Advanced Materials Research*, **239-242**, 2628 (2011)
2. J. Koo, J. H. Jang, B. S. Bae, *J. Mater. Res.*, **16**, 430 (2001)
3. P. B. Jamieson, S. C. Abrahams, J. L. Bernstein. *J. Chem. Phys.*, **48**, 5048 (1968)
4. A.M. Glass, *J. Appl. Phys.*, **40**, 4699 (1969)
5. J. D. Zook, S. T. Liu, *J. Appl. Phys.*, **49**, 4604 (1978)
6. S. Sakamoto, T. Yazaki, *Appl. Phys. Lett.*, **22**, 429-431 (1973)
7. M. Horowitz, A. Bekker, B. Fischer, *Appl. Phys. Lett.*, **62**, 2619 (1993)
8. S. Nishiwaki, J. Takahashi, K. Kodaira, M. Kishi, *Jap. J. Appl. Phys.*, **35**, 5137 (1996)
9. Y. Xu, C. J. Chen, R. Xu, J. D. Mackenzie, *Phys. Review B*, **44**, 35 (1991)
10. S. S. Thöny, K. E. Youden, J. S. Harris Jr., L. Hesselink, *Appl. Phys. Lett.*, **65**, 2018-2020 (1994)
11. M. Lee, R. S. Feigelson, *J. Crystal Growth*, **180**, 220 (1997)
12. R. G. Mendes, E. B. Araújo, H. Klein, J. A. Eiras, *J. Materials Sc. Letters*, **8**, 1941 (1999)
13. F. H. Wanga, C. F. Yang, M. C. Liu, *J. Sci. Innovation*, **6**, 7 (2016)
14. Y. K. Wang, T. Y. Tseng, and L. Pang, *Appl. Phys. Lett.*, **80**, 3790 (2002)
15. R. Balachandran, B. H. Ong, H. Y. Wong, K. B. Tan, M. Muhamad Rasat, *Inter. Jour. Electrochem. Sci.*, **7**, 11895 (2012)